Deep learning approach for high-accuracy electron counting of MAPS-type direct electron detectors at increased electron dose

Jingrui Wei^a, Kalani Moore^b, Benjamin Bammes^b, Barnaby D.A. Levin^b, Nicholas Hagopian^a, Ryan Jacobs^a, Dane Morgan^a and Paul M. Voyles^{a,*}

^{a.} Department of Materials Science and Engineering, University of Wisconsin-Madison,
Madison, Wisconsin, United States of America

b. Direct Electron L.P., San Diego, CA, United States of America

* paul.voyles@wisc.edu

Abstract

Electron counting can be performed algorithmically for monolithic active pixel sensor direct electron detectors to eliminate readout noise and Landau noise arising from the variability in the amount of deposited energy for each electron. Errors in existing counting algorithms include mistakenly counting a multi-electron strike as a single electron event, and inaccurately locating the incident position of the electron due to lateral spread of deposited energy and dark noise. Here, we report a supervised deep learning approach based on Faster R-CNN to recognize single electron events at varying electron doses and voltages. The deep learning approach shows high accuracy according to the near-ideal modulation transfer function and detector quantum efficiency for sparse images. It predicts, on average, 0.47 pixel deviation from the incident positions for 200 kV

electrons versus 0.59 pixel using the conventional counting method. The deep learning approach also shows better robustness against coincidence loss as the electron dose increases, maintaining the MTF at half Nyquist frequency above 0.83 as the electron density increases to 0.06 e⁻ / pixel. Thus, the deep learning model extends the advantages of counting analysis to higher dose rates than conventional methods.

Keywords: transmission electron microscopy, direct detector, electron counting, low-dose, neural network, object detection, deep learning

1. Introduction

Direct electron detectors have been rapidly developed and widely applied in both materials and biological transmission electron microscopy (TEM). Compared to scintillator-coupled cameras, direct detectors expose their radiation-hardened sensor directly to the electron beam and avoid the inefficiency inherent in electron-to-photon conversion in a scintillator-coupled system, enabling direct detectors to achieve high signal-to-noise ratio (SNR) equal to or better than that of film (McMullan et al. 2014). A direct detector used in electron microscopy should have a high SNR for single electrons, especially for low-dose imaging of beam-sensitive materials such as biomaterials (Li, Mooney, et al. 2013) or metal-organic frameworks (MOFs) (Peng et al. 2022). High single-electron SNR is also vital for fast acquisition during *in situ* TEM or 4D scanning TEM (STEM). This aspect of performance can be characterized by detector quantum efficiency (DQE) (Meyer and Kirkland 2000), which is defined as the ratio of the squares of the output and input image SNR. Ideally, a direct detector would offer high spatial resolution imaging to preserve spatial details from the incident electrons. This can be characterized by modulation transfer function (MTF) (De Ruijter 1995), which is defined as the Fourier transform of the real-space point spread

function. Ideally, a direct detector would also maintain good performance over a wide range of primary electron beam voltages, which would facilitate imaging different types of specimens.

There are two common types of TEM direct detectors: monolithic active pixel sensors (MAPS) and hybrid pixel array detectors (HPADs). MAPS detectors are devices in which the readout electronics are implemented within the same semiconductor wafer as the detecting layer, while HPADs consist of a much thicker detecting layer that is fabricated separately and subsequently bump bonded to an application specific integrated circuit (ASIC) (Levin 2021).

HPADs, such as Medipix-based detectors (Mir et al. 2017), the EMPAD (Tate et al. 2016) and the DECTRIS ELA (Plotkin-Swing et al. 2020) have relatively wide, thick pixels designed to fully stop incoming electrons. The lateral spread of electrons across multiple pixels in these detectors is minimized at lower electron beam voltages (i.e., 100 kV and lower), but becomes more important at 200 and 300 kV. Sensors fabricated from high atomic number materials (Paton et al. 2021) have been employed by some HPADs to minimize the lateral spreading of high energy electrons.

MAPS detectors, such as the DE-64 (Mendez et al. 2019), K3 (Sun et al. 2021), Falcon4 (Nakane et al. 2020), have relatively small, thin pixels, designed to sample the energy of incoming electrons without fully stopping them. This allows for a greater density of pixels on the sensor, enabling high-resolution imaging at fixed magnification. The lateral spread of electrons across multiple pixels on a MAPS detector is minimized by optimizing the sensitive layer thickness for a particular range of primary electron beam voltages, typically 200 and 300 kV (Levin 2021), but some electrons still generate signal in several pixels. Many MAPS direct electron detectors operate in integrating mode, where the charge generated by all primary electrons interacting with a pixel within the frame time is accumulated to form the output. A commonly used alternative operating

mode is counting mode, where the electron beam intensity is limited so that the signal deposited by each incident electron is individually distinguishable as a separate "electron event". In counting mode, each camera frame is processed via software to identify each electron event and output a single "count" in the corresponding estimated location of the incident electron on the sensor. Counting mode normalizes the intensity of each detected electron, eliminating noise arising from the intrinsic variations in the deposition of energy by primary electrons (Landau noise), dramatically improving DQE, along with enabling super-resolution readout if localization of each electron event is performed with sub-pixel precision (Li, Zheng, et al. 2013). It also allows compression of datasets from digital readout to low bit electron counts, minimizing storage and computer memory requirements. However, the performance of existing counting algorithms (Battaglia et al. 2009; G McMullan et al. 2009; Datta et al. 2021) is limited due to the inherent randomness of electron scattering through the sensor. First, there is significant room for improvement in the accuracy of localizing the point of incidence of an electron within a cluster of illuminated pixels, which would further improve resolution and MTF. Second, it is challenging to distinguish multiple electron events occurring close to one another from a single electron event covering several pixels. When two or more electrons are counted as one—a phenomenon known as coincidence loss—signal is lost, reducing sensitivity and DQE.

Deep learning methods are a promising approach to image analysis tasks like electron counting. Convolutional neural networks (CNNs) have been used for tasks ranging from image classification to objection detection and segmentation across a number of technical or scientific fields including autonomous vehicles (Grigorescu et al. 2020), medical image processing (Wang et al. 2021), and image analysis in material science (Jacobs 2022). van Schayck *et al.* trained a CNN to reconstruct the incident position of electrons for the Timepix3 HPAD detector (van Schayck et al. 2020). The

Timepix3 events created by 300 kV electrons on a 500 μ m thick sensor are quite large, covering up to 12 × 12 physical pixels of size 55 μ m, which significantly degrades the detector performance. The CNN improved determination of the incident electron position, resulting in significant improvement of the MTF (van Schayck et al. 2020) compared to conventional counting methods. This work shows that the deposited energy pattern of a primary electron, even though generated by a stochastic electron trajectory, contains 2D features that a CNN can learn.

Here, we present a deep learning (DL) model trained to recognized electron events for a Celeritas XS direct electron detector (Direct Electron LP, San Deigo, CA, USA) and compare the counting performance of the DL model with a conventional method, connected component labeling (CCL) (He et al. 2017). The Celeritas XS camera (Chatterjee et al. 2021) is a 1024 x 1024 pixel MAPS direct detector with 15 µm pixel size, optimized for high frame rate readout and high dynamic range imaging for 4D STEM. Frame rates of up to 87 kHz can be achieved by reducing the physical readout area on the sensor down to 256 × 64 pixels. This ultrafast capability enables 4D STEM acquisition at similar scan speeds to conventional STEM. When compared to slower MAPS detectors, the fast frame rate of Celeritas XS results in a sparser signal in each frame at a fixed electron dose.

The electron event sizes for the Celeritas XS in this study are small, and, as shown below, the incident positions are close to the peak intensity positions. Thus, we focus on recognizing single electron events within the frame instead of localizing the electron strike position within the event. The model is trained on simulated Celeritas XS data and tested on experimental Celeritas XS data. It adopts the popular object detection neural network Faster R-CNN due to its high accuracy especially for small objects (Ren et al. 2017). The model performance is characterized using the MTF, DQE, and other evaluation metrics on images with different electron densities. Finally, we

illustrate model performance by applying it to ptychographic imaging of a 2D material and 4D STEM strain mapping of SrTiO₃. The DL model allows accurate electron counting at higher electron dose rates than CCL. Although these results are specific to the Celeritas XS detector, a similar approach should extend the benefits of counting to higher electron dose for other MAPS direct detectors as well.

2. Methods

2.1 Electron trajectory and detector readout simulation

Supervised learning of a neural network requires training data with known ground truth. In this case, that means electron images where the position of every electron strike is known. Unfortunately, this data is not available from experiments. Due to the randomness of energy deposition in the sensor, the "true" electron strike position is not just unknown but unknowable. Therefore, we turn to simulations to create the required training data.

Individual electrons impacting the Celeritas XS sensor were simulated using pyPenelope software (Salvat et al.). The 'shower' package with default parameters was used to simulate 100,000 primary electron trajectories for 80 kV and 55,000 electrons for 200 kV, impacting a multi-layer material that matches the physical design of the sensor from Direct Electron. A Gaussian blur was added to the location of the energy deposited to account for diffusion within the epitaxial layer, and custom Python code was used to translate the energy deposited in the epitaxial layer by the electron trajectories into pixel values representing an electron event on Celeritas XS. Figure 1 shows that the distributions of event energies and event sizes for simulated events were comparable to experimental events. The somewhat poorer agreement of the size distributions may reflect

limitations in the experimental identification of events, rather than limitations of the simulations. The same parameters were used for 80 kV and 200 kV simulations. The position of the electron impacts was randomly distributed within the central pixel of the electron event. Example event images are shown in Figure 1(c, f) for 200 and 80 kV respectively.

2.2 Experimental data

A Thermo Fisher Titan STEM equipped with a CEOS probe aberration corrector was used to collect datasets for the characterization of counting algorithms. The microscope was operated at 200 kV and 80 kV in TEM mode. The Celeritas XS detector was operated in rolling shutter mode with an adjustable readout area of the 1024 x 1024 pixel sensor. Uniformly illuminated frames were collected at different frame rates for noise power spectrum calculations and a beam stop was used to introduce a silhouette for MTF calculations.

A 4D-STEM dataset of monolayer WS₂ for ptychography reconstruction was acquired with a convergence semi-angle of 16.7 mrad, a C2 aperture sized 50 μm, and a camera length of 160 mm. The electron probe current was 7.5 pA and the scan step size was 0.14 Å. The Celeritas XS detector acquired frames synchronously with the probe scanning with a frame rate of 7385 Hz. The total electron dose for each exposure is about 10⁴ e⁻ Å⁻², and the electron density of the bright field region of each diffraction pattern is 0.04 e⁻/pixel. Another ptychography dataset was collected under similar experiment parameters, except that the frame rate is 1959 Hz, which gives a much higher electron density of 0.15 e⁻/pixel. A 4D-STEM dataset of SrTiO₃[001] was acquired for lattice parameter measurement with a convergence semi-angle of 1.3 mrad. The electron probe scanned across a uniform area with a step size of 1.7 Å and dwell time of 2 ms. The electron dose for each exposure is about 400 e⁻ per frame.

2.3 Faster R-CNN model for electron event recognition

We trained a Faster R-CNN (Ren et al. 2017) model using TorchVision (maintainers and contributors 2016) as the backend. Faster R-CNN, as the popular two-stage object detection algorithm, stands out at detection and localization accuracy especially for small objects compared to other single-shot algorithms, such as the You Only Look Once (YOLO) and Single Shot Detector (SSD) methods (Liu et al. 2021). Despite the faster inference speed of single-shot algorithms, the need for high accuracy in electron event recognition and precise bounding boxes makes Faster R-CNN the optimal choice. We have also explored semantic segmentation methods. A U-Net (Ronneberger et al. 2015) model was trained to classify each pixel into zero-electron, one-electron, and multiple-electron classes. The trained U-Net missed more electrons compared to the conventional counting algorithm as electron density started to increase. It became evident that the basic U-Net model was insufficient for this complex task, where the size and shape variation of the objects arises from a combination of random electron trajectories and overlapping electron events, and image contrast significantly varies as electron density changes.

Our modified Faster R-CNN structure is shown in Figure 2(a). Compared to natural images usually analyzed using Faster R-CNN, the detector readout image contains less complicated features but a much larger number of very small objects to be recognized. We modified the backbone, anchors, and hyperparameters of the model accordingly. A simple 4-convolutional-layer backbone was used to generate feature maps, excluding any down-sampling operation in the backbone to preserve high-resolution features. The region proposal network (RPN) was trained to generate object region proposals based on feature maps and predefined shapes, *i.e.* anchors. We chose the four anchor shapes shown in Figure 2 based on the dominant event sizes on the Celeritas XS detector (Figure 1). The subsequent non-maximum suppression (NMS) (Neubeck and Van Gool 2006) selects a

single proposal from many overlapping proposal candidates based on a threshold of intersection over union (IoU). Then, a region-of-interest (ROI) pooling layer extracts a fixed-length feature vector from the feature maps for each object proposal and feeds it into the classifier. The classifier is composed of fully connected layers that finally branch into two sibling output layers: one that produces softmax probability estimates for the electron event object class and background class and another layer that outputs four real-valued numbers as the refined bounding boxes for each class. Table 1 summarizes the hyperparameters of the Faster R-CNN model which were optimized based on preliminary observations of model performance.

The model was trained on ~8000 simulated detector readout images of varying electron densities between $0.002 \sim 0.1$ e^{-/}pixel. Most of the Celeritas XS electron events are less than 4 pixels (Figure 1). An eligible proposed impact region from the RPN that is only one pixel off the ground truth could therefore result in an extremely low IoU score, which would be undesirably filtered out and mislead the model training. To avoid this problem, the images were up-sampled by a factor of 2 before being used for training to make the objects larger and easier to detect. We used the 4-step alternating training as described in (Ren et al. 2017). Aggregation loss (Zhang et al. 2018) was used for each step to force proposals to be compactly located to the corresponding objects, so that real neighboring events are not filtered out by NMS. The training parameters are also listed in Table 1. One set of final weights was saved after training on 200 keV data and another set was saved after training on 80 keV data.

Figure 2(b) shows the workflow for using the model to count electrons in an image. The raw image is first up-sampled and divided into equal-sized patches using overlapping windows, as the model performs better when the input size is close to that of the training dataset, and the computation complexity scales up with the square of the input image size (Wu 2018). Overlapping windows

are used to capture events that might otherwise cross a window boundary. Each window is separately fed into the Faster R-CNN to generate the bounding boxes. To guide the model towards more accurate detection at different electron density levels, the hyperparameters annotated as 'tuned' in Table 1 are tuned based on the number of electrons estimated from the total digital counts within the window, which is calculated from the total intensity and the known mean single event intensity. After down-sampling the detected boxes and assigning incident positions to the peak intensity pixels within each box (as discussed in Section 3.1), the generated image patches are stitched together to produce the final counted image.

2.4 Evaluation metrics

For experimental detector readout images, MTF and DQE are the primary characterization metrics. The MTF was calculated by FindDQE (Ruskin et al. 2013) using the beam stop silhouette method, and it accounts for lost counts at low resolution. The DQE was calculated as (G. McMullan et al. 2009)

$$DQE = DQE(0)\frac{MTF^{2}(\omega)}{NNPS(\omega)},$$

where the DQE(0) was estimated using the noise binning method, and the NNPS(ω) is the normalized noise power spectrum calculated from the FFT of a uniformly illuminated image. Two sets of experimental images were used to measure MTF/DQE. One set was collected at a vanishingly low electron density, and the other set was collected at much higher density. The relative detector conversion efficiency (DCE) was used to describe the coincidence loss (Li, Zheng, et al. 2013) at different doses. DCE is defined as the ratio of input and detected electron counts and is normalized by the ratio at a very low electron dose. The absolute electron dose for

experimental data is not reported since our microscope does not have a Faraday cage detector, but a series of images of proportionally increasing dose can be obtained by proportionally increasing the exposure time under identical beam conditions, giving a concrete trend of the coincidence loss.

For simulated data with known ground truth of electron hits, position deviation, recall, precision, and F1 score were measured to evaluate the model performance. Position deviation is the root mean square (RMS) error between detected electron incident positions and the ground truth positions in units of pixels. Instead of defining the recall or precision based on an IoU threshold as is typical for object detection problems, we combined the recognition and localization steps together and set the criteria for detection to be an event found within one pixel of the ground truth position.

The deep learning model was benchmarked against the state-of-the-art CCL method implemented using the SciPy Ndimage library. Both methods were characterized using the same datasets and metrics.

3. Results and discussion

3.1 Optimum incident electron event localization method

Once electron events are recognized, we must select a pixel within the event as the position of the incident electron. For Celeritas XS, the pixel with the maximum intensity is the best choice. Figure 3 compares the accuracy of three common electron event localization methods, centroid, binarized

centroid, and maximum intensity, applied to the simulated electron event data. The centroid method calculates the geometric center of a cluster where each pixel has been weighted according to their intensity values. The binarized centroid method calculates the centroid after thresholding and binarization, so that all pixels above the noise threshold level have an equal weight of 1 regardless of their intensity. The maximum method assigns the incident position to the pixel with highest intensity. For 200 kV simulated electron events, a larger proportion of position deviations of the maximum method fall within one pixel compared to the other two methods. For 80 kV electrons, there is no significant difference in the accuracy of these methods, so the maximum method is selected because it requires the least computation. Approximately 75 to 90% of the predictions of the maximum method show error within 1 pixel, making it an excellent electron localization method for the Celeritas XS detector.

3.2 Accuracy of the deep learning counting approach

Figure 4 shows the performance characterization of the deep learning approach versus CCL. At 200 keV, the voltage for which the detector is optimized, the counting mode MTF calculated from sparse experimental images is already very close to ideal using CCL counting. However, the MTF at Nyquist frequency is improved to 0.63 by the DL model vs. 0.60 by CCL (The ideal value is 0.637). The sharp drop in MTF at low frequency that occurs in the CCL counting and integrating mode does not occur in the DL model, indicating that the model is less affected by the intensity clusters contributed by electrons scattered to large lateral distances from their incident positions. The averaged electron event size from the DL model is 2.06 pixels vs. 2.88 pixels from CCL, also showing that the DL model distinguishes overlapping electron events better than CCL. The DL model MTF remains higher at high frequency due to its high accuracy of finally locating the incident positions. The averaged position deviation (Figure 4c), calculated from simulated frames

with known ground truth, is slightly lower for the DL model than CCL, consistent with the modest improvement in experimental MTF. The DQE for the DL model and CCL are also quite close to each other, although the DL model only falls to 0.37 at the Nyquist frequency *vs.* 0.34 for CCL. The DQE results indicate that no extra noise is induced by the DL model detection.

At 80 keV, the DL model provides similar incremental improvement over CCL for sparse images. At lower voltage, the lateral spread of electrons in the thin sensitive layer of a MAPS detector is larger than at higher voltages (Levin 2021). For the Celeritas XS detector, the mean 80 keV electron event size is 3.4 pixels, compared to 2.3 pixels for 200 keV. The DL model improves event recognition, but it does not improve the accuracy of identifying the pixel struck by the electron. Therefore, it offers limited improvement in MTF at the highest spatial frequencies (above 0.75 Nyquist) and position deviation compared to CCL.

The DL model shows high robustness against electron energy variations for the Celeritas XS detector. When tested on 80 keV data, we found that the model trained on only 200 keV data gives a similar MTF, DQE, and other performance metric scores as those obtained using a model trained on 80 keV data. The difference in event intensities at different voltages is interpreted by the model in the total electron counts estimation step. The moderately different event size distributions at different voltages do not cause significant domain shift and are equally well recognized by the model. When migrating the DL approach for other detectors that have a significant difference in event size at different voltages, it will be necessary to use training data at the specific voltage to achieve best performance.

3.3 Robustness of performance at higher electron dose

Figure 5 illustrates the performance of the DL model at increased electron density using both simulated and experimental data. Figure 5(a)-(c) evaluates performance on simulated images. For typical sparse images for electron counting (below 0.02 e⁻/pixel), the DL model and the CCL perform almost identically, with the DL model giving slightly higher recall and CCL giving slightly higher precision, resulting in similar F1 scores. As the electron dose increases, the DL model maintains the high precision and increasingly better recall, thus keeping the F1 score above 0.75 at 0.1 e-pixel and sparser. Figure 5(d)-(g) evaluates performance on experimental data. The relative DCE in Figure 5d is in good agreement with the trend of recall in Figure 5(a). Figure 5(e)-(f) shows MTF, NPS, and DQE for data with an electron density of 0.06 e⁻/pixel. Neither the DL model nor CCL MTF reaches 1 at low frequencies due to lost counts, i.e. coincidence loss (Li, Zheng, et al. 2013), but the DL model MTF is higher at all frequencies. Higher NPS also arises from the reduced coincidence loss of the DL model. The DL model DQE remains as high as the low dose DQE in Figure 4b. Based on the robustness of the DL model at high electron dose and the fast readout speed of Celeritas XS, ~ 0.06 e⁻/pixel represents $120 \sim 5000$ e⁻/pixel/s, which is at least ten times higher than the maximum counting rate of other MAPS detectors operating in onthe-fly counting mode (Nakane et al. 2020; Sun et al. 2021; Peng et al. 2023). For counting and integrating mode, the tradeoff between high DQE and no coincidence loss always exists, even though it is less concerning when using the DL model as shown in Figure 5(e-g). At even higher electron dose, the choice between integrating and DL model counting could depend on the information needed at different frequencies for specific datasets.

3.4 Validation on experimental 4D STEM data

Ptychographic Phase reconstruction

Ptychographic phase reconstruction from CBED patterns benefits from the interference between the diffracted beams and the zero beam, but the zero beam can be too bright for counting mode on MAPS detectors. We applied the CCL counting method and the DL model to a 4D STEM dataset of monolayer WS2 and compared the reconstructed phase images using the Wigner distribution deconvolution (WDD) (Rodenburg and Bates 1992) or single side band (SBB) (Pennycook et al. 2015) implemented in the pyptychoSTEM software (Tim Pennycook & Christoph Hofer 2021), as shown in Figure 6. The phase images generated from the counted datasets show better quality than phase images generated from uncounted data, as indicated by the cleaner background of the embedded diffractograms in Figure 6(b) and (c) vs. Figure 6(a). With less noise transferred from the detector readout, the counted datasets resolve many atoms better as highlighted by the color boxes in Figure 6 (a-c). The absolute phase is lower for the counted datasets due to coincidence loss, which has a more significant effect on the CCL counted data than the DL model counted data (Figure 6d), consistent with the characterization results in Section 3.2.

We have also performed the same comparison using a dataset that is collected at a higher electron dose (~0.15 e/pixel), which is challenging for conventional counting techniques. Not surprisingly, the phase image reconstructed from the CCL counted dataset is strongly affected by the low MTF/DQE and shows poor contrast. The DL model retains the fidelity of localizing electron events and shows lower contrast than the integrating dataset, but the reconstruction is still of a reasonably good quality. For images with a high local intensity variance, it has been difficult to determine a suitable boundary between the area with sufficient sparsity for counting and the area that is not sparse enough for counting. The DL model with its proven larger applicable dose (sparsity) range will be a useful counting algorithm that smoothes out the boundaries and works almost equally well at local areas with different electron densities.

Strain measurement

Counting also improves strain measurements of a 4D STEM dataset with a low convergence angle, which can be expected from its higher MTF according to quantitative study by Christoph Mahr *et. al.* (Mahr et al. 2015) Figure 7 compares 4D STEM data from unstrained SrTiO₃ [001] processed with DL model counting and in integrating mode without counting. The electron density inside the zero disk is about 0.3 e⁻/pixel. The conventional CCL method failed at this relatively high electron density, yielding counted images that show no disk features at all. However, Figure 7 shows that the DL counting method can work at this dose, and, due to the elimination of Landau noise, the diffraction disks can be resolved much more clearly using DL model counting than using integrating mode.

We measured the lattice parameter at each probe position by summing ten frames and applying cross correlation with a disk template. The cross correlation located at least two more diffraction disks from the DL model counted frames than from the integrating frames. The standard deviation of the lattice measurements is 0.050 Å for the integrating mode dataset and 0.039 Å after processing the data using the DL counting model. This demonstrates that the DL model will be helpful in improving the precision of strain measurement from a low dose noisy dataset that is insufficiently sparse for conventional counting. Tolerance for noisy data allows faster data acquisition to characterize larger areas or reduce specimen drift.

3.5 Discussion and outlook

Compared with CCL, the computational complexity of the deep learning approach is much higher. Most of the computation time is contributed by NMS, which usually computes a large IoU matrix of $10^2 \sim 10^3$ proposals because of the large number of tiny objects that need to be detected.

Counting electrons in a 256 × 256 image at 0.05 e⁻/pixel took about 10 s on a single Intel Xeon E5-2670 (2.3GHz) CPU processor with a single thread. Running it on a single GPU (Tesla M10) doubled the computation speed. The computation time is roughly proportional to the total number of pixels and slightly increases when counting denser images. This makes the DL model suitable for post-acquisition analysis but not for live session processing. Multi-CPU and multi-GPU processing would reduce the computation time. The latest YOLOv8 nano object version (Jocher et al. 2023) might be a promising base architecture to achieve higher speed as well as good accuracy of locating small objects.

Due to differences in the characteristics of the detectors and event sizes involved, a direct comparison of our DL counting method for Celeritas XS and the results achieved by van Schayck *et al.* for the Timpix3 detector with the trained CNN is challenging, but we note that the absolute positional accuracy of both methods is comparable. Because of the small event size of the Celeritas XS detector, a greater proportion of electron strikes are well-located with zero deviation than was the case for van Schayck *et al.* However, the outliers of the deviation distribution are about 1 pixel larger due to false positive detections. These two sides of the performance of DL counting method compensate for each other and result in similar mean position deviation compared to the Timepix3 CNN (0.47 pixels *vs.* 0.50 pixels). For potential implementation for other similar detectors, if the average event size is large, *e.g.* more than 4 square pixels, adding an additional CNN branch to the DL model for locating the incident positions within the predicted boxes of electron events might be helpful to further improve the electron localization accuracy.

A hybrid counting approach (Bammes et al. 2019) has been developed to overcome the challenge of limited dynamic range of MAPS detectors. The hybrid counting approach generates a binary mask corresponding to the area that is sparse enough for counting, performing electron counting

in sparse regions and charge integration in non-sparse regions. For datasets that contain both large intense and diffuse areas, for example, the bright-field disk and dark-field region, the hybrid counting approach achieves high SNR in the dark-field while preserving information from the bright-field disk. If the hybrid counting approach is built based on DL counting, the binary mask of sparse area can be significantly expanded towards higher electron density area, further improving the averaged SNR over the intense and diffuse areas.

Although we have not explored them here, it is interesting to speculate on the potential benefits of DL counting for biological electron microscopy. Improvements in MTF and DQE may improve data quality in, for example, single-particle cryo-electron microscopy. For applications that can sustain and benefit from higher dose, such as plastic section tomography, extending counting to higher dose may be a significant benefit.

4. Conclusion

The deep learning model trained to recognize single electron events in Celeritas XS detector readout images extends the benefits of counting mode to higher electron density than conventional counting methods. It reduces coincidence losses by improved recognition of nearby electron events, achieving MTF of 0.83 and DQE of 0.76 at half Nyquist frequency even at the relatively high electron dose of 0.06 e⁻/pixel. The DL model has allowed us to generate a ptychographic reconstruction at a dose level of 0.15 e⁻/pixel, and precisely measure diffraction disk positions at a dose level of 0.3 e⁻/pixel, whereas a conventional counting algorithm fails at these dose levels. The deep learning model also shows small improvements in performance for counting very sparse images compared to conventional methods, achieving very high MTF and DQE. The DL model

requires dramatically higher computation than conventional methods, and the current implementation is therefore more appropriate as a post-processing technique than a real-time imaging technique. By enabling electron counting with a higher electron dose incident on the detector, the DL model provides greater flexibility for experiment design and can be used to improve results from 4D STEM techniques such as ptychographic imaging and strain mapping. Although this model is specific to the Celeritas XS detector, the general approach of training a deep learning model and applying it to electron counting should be beneficial for other similar direct detectors.

Data availability

The simulated training and test datasets is available via the Foundry-ML (Blaiszik et al. 2022) service at DOI: 10.18126/rgew-xbw4. Experimental data is available via the Materials Data Facility (DOI: 10.18126/xv6r-y3lr). All codes, including the saved model and an example Jupyter notebook showing how to load the data and implement the model from Foundry-ML are available at https://github.com/wdwzyyg/ElectronCounting.git.

Acknowledgments

This work was primarily supported by the National Science Foundation project "Collaborative Research: Framework: Machine Learning Materials Innovation Infrastructure" (UW-Madison: OAC-1931298, U. Chicago OAC-1931306). The detector readout simulations by K. M., B. B., and

B.D.A.L. were supported by DOE Office of Science Award DE-SC0018493. Experiments were performed using facilities supported by the Wisconsin MRSEC (DMR-1720415).

Reference

Bammes B, Ramachandra R, Mackey MR, Bilhorn R, Ellisman M. 2019. Multi-Color Electron Microscopy of Cellular Ultrastructure Using 4D-STEM. Microsc Microanal. 25(S2):1060–1061. doi:10.1017/S1431927619006032. https://doi.org/10.1017/S1431927619006032.

Battaglia M, Contarato D, Denes P, Giubilato P. 2009. Cluster imaging with a direct detection CMOS pixel sensor in Transmission Electron Microscopy. Nucl Instruments Methods Phys Res Sect A Accel Spectrometers, Detect Assoc Equip. 608(2):363–365.

doi:10.1016/j.nima.2009.07.017. http://dx.doi.org/10.1016/j.nima.2009.07.017.

Blaiszik B, Scourtas A, Schmidt K. 2022. Foundry. https://github.com/MLMI2-CSSI/foundry.

Chatterjee D, Wei J, kvit A, Bammes B, Levin B, Bilhorn R, Voyles P. 2021. An Ultrafast Direct Electron Camera for 4D STEM. Microsc Microanal. 27(S1):1004–1006. doi:10.1017/S1431927621003809.

Datta A, Ng KF, Balakrishnan D, Ding M, Chee SW, Ban Y, Shi J, Loh ND. 2021. A data reduction and compression description for high throughput time-resolved electron microscopy. Nat Commun. 12(1):1–15. doi:10.1038/s41467-020-20694-z.

Grigorescu S, Trasnea B, Cocias T, Macesanu G. 2020. A survey of deep learning techniques for autonomous driving. J F Robot. 37(3):362–386. doi:https://doi.org/10.1002/rob.21918.

https://doi.org/10.1002/rob.21918.

He L, Ren X, Gao Q, Zhao X, Yao B, Chao Y. 2017. The connected-component labeling problem: A review of state-of-the-art algorithms. Pattern Recognit. 70:25–43. doi:https://doi.org/10.1016/j.patcog.2017.04.018.

https://www.sciencedirect.com/science/article/pii/S0031320317301693.

Jacobs R. 2022. Deep learning object detection in materials science: Current state and future directions. Comput Mater Sci. 211(May):111527. doi:10.1016/j.commatsci.2022.111527. https://doi.org/10.1016/j.commatsci.2022.111527.

Jocher G, Chaurasia A, Qiu J. 2023. YOLO by Ultralytics.

https://github.com/ultralytics/ultralytics.

Levin BDA. 2021. Direct detectors and their applications in electron microscopy for materials science. JPhys Mater. 4(4). doi:10.1088/2515-7639/ac0ff9.

Li X, Mooney P, Zheng S, Booth CR, Braunfeld MB, Gubbens S, Agard DA, Cheng Y. 2013. Electron counting and beam-induced motion correction enable near-atomic-resolution single-particle cryo-EM. Nat Methods. 10(6):584–590. doi:10.1038/nmeth.2472.

Li X, Zheng SQ, Egami K, Agard DA, Cheng Y. 2013. Influence of electron dose rate on electron counting images recorded with the K2 camera. J Struct Biol. 184(2):251–260. doi:10.1016/j.jsb.2013.08.005. http://dx.doi.org/10.1016/j.jsb.2013.08.005.

Liu Y, Sun P, Wergeles N, Shang Y. 2021. A survey and performance evaluation of deep learning methods for small object detection. Expert Syst Appl. 172:114602.

doi:10.1016/J.ESWA.2021.114602.

Mahr C, Müller-Caspary K, Grieb T, Schowalter M, Mehrtens T, Krause FF, Zillmann D, Rosenauer A. 2015. Theoretical study of precision and accuracy of strain analysis by nano-beam electron diffraction. Ultramicroscopy. 158:38–48. doi:10.1016/j.ultramic.2015.06.011. http://dx.doi.org/10.1016/j.ultramic.2015.06.011.

maintainers T, contributors. 2016. TorchVision: PyTorch's Computer Vision library. GitHub Repos.

McMullan G., Chen S, Henderson R, Faruqi AR. 2009. Detective quantum efficiency of electron area detectors in electron microscopy. Ultramicroscopy. 109(9):1126–1143. doi:10.1016/j.ultramic.2009.04.002.

McMullan G, Clark AT, Turchetta R, Faruqi AR. 2009. Enhanced imaging in low dose electron microscopy using electron counting. Ultramicroscopy. 109(12):1411–1416. doi:https://doi.org/10.1016/j.ultramic.2009.07.004.

https://www.sciencedirect.com/science/article/pii/S0304399109001703.

McMullan G, Faruqi AR, Clare D, Henderson R. 2014. Comparison of optimal performance at 300keV of three direct electron detectors for use in low dose electron microscopy.

Ultramicroscopy. 147:156–163. doi:10.1016/j.ultramic.2014.08.002.

http://dx.doi.org/10.1016/j.ultramic.2014.08.002.

Mendez JH, Mehrani A, Randolph P, Staggb S. 2019. Throughput and resolution with a next-generation direct electron detector. IUCrJ. 6:1007–1013. doi:10.1107/S2052252519012661.

Meyer RR, Kirkland AI. 2000. Characterisation of the signal and noise transfer of CCD cameras for electron detection. Microsc Res Tech. 49(3):269–280.

doi:https://doi.org/10.1002/(SICI)1097-0029(20000501)49:3<269::AID-JEMT5>3.0.CO;2-B. https://doi.org/10.1002/(SICI)1097-0029(20000501)49:3%3C269::AID-JEMT5%3E3.0.CO.

Mir JA, Clough R, MacInnes R, Gough C, Plackett R, Shipsey I, Sawada H, MacLaren I, Ballabriga R, Maneuski D, et al. 2017. Characterisation of the Medipix3 detector for 60 and 80 keV electrons. Ultramicroscopy. 182:44–53. doi:10.1016/j.ultramic.2017.06.010. http://dx.doi.org/10.1016/j.ultramic.2017.06.010.

Nakane T, Kotecha A, Sente A, McMullan G, Masiulis S, Brown PMGE, Grigoras IT, Malinauskaite L, Malinauskas T, Miehling J, et al. 2020. Single-particle cryo-EM at atomic resolution. Nature. 587(7832):152–156. doi:10.1038/s41586-020-2829-0. https://doi.org/10.1038/s41586-020-2829-0.

Neubeck A, Van Gool L. 2006. Efficient Non-Maximum Suppression. In: 18th International Conference on Pattern Recognition (ICPR'06). Vol. 3. p. 850–855.

Paton KA, Veale MC, Mu X, Allen CS, Maneuski D, Kübel C, O'Shea V, Kirkland AI, McGrouther D. 2021. Quantifying the performance of a hybrid pixel detector with GaAs:Cr sensor for transmission electron microscopy. Ultramicroscopy. 227(February). doi:10.1016/j.ultramic.2021.113298.

Peng R, Fu X, Mendez JH, Randolph PS, Bammes BE, Stagg SM. 2023. Characterizing the resolution and throughput of the Apollo direct electron detector. J Struct Biol X. 7:100080. doi:https://doi.org/10.1016/j.yjsbx.2022.100080.

https://www.sciencedirect.com/science/article/pii/S2590152422000216.

Peng X, Pelz PM, Zhang Q, Chen P, Cao L, Zhang Y, Liao H-G, Zheng H, Wang C, Sun S-G, et al. 2022. Observation of formation and local structures of metal-organic layers via complementary electron microscopy techniques. Nat Commun. 13(1):5197. doi:10.1038/s41467-022-32330-z. https://doi.org/10.1038/s41467-022-32330-z.

Pennycook TJ, Lupini AR, Yang H, Murfitt MF, Jones L, Nellist PD. 2015. Efficient phase contrast imaging in STEM using a pixelated detector. Part 1: Experimental demonstration at atomic resolution. Ultramicroscopy. 151:160–167. doi:10.1016/j.ultramic.2014.09.013.

Plotkin-Swing B, Corbin GJ, De Carlo S, Dellby N, Hoermann C, Hoffman M V, Lovejoy TC, Meyer CE, Mittelberger A, Pantelic R, et al. 2020. Hybrid pixel direct detector for electron energy loss spectroscopy. Ultramicroscopy. 217:113067.

doi:https://doi.org/10.1016/j.ultramic.2020.113067.

https://www.sciencedirect.com/science/article/pii/S0304399120302187.

Ren S, He K, Girshick R, Sun J. 2017. Faster R-CNN: Towards Real-Time Object Detection with Region Proposal Networks. IEEE Trans Pattern Anal Mach Intell. 39(6):1137–1149. doi:10.1109/TPAMI.2016.2577031.

Rodenburg J, Bates RHT. 1992. The theory of super-resolution electron microscopy via Wigner-distribution deconvolution. Philos Trans R Soc London Ser A Phys Eng Sci. 339:521–553.

Ronneberger O, Fischer P, Brox T. 2015. U-net: Convolutional networks for biomedical image segmentation. Lect Notes Comput Sci (including Subser Lect Notes Artif Intell Lect Notes Bioinformatics). 9351:234–241. doi:10.1007/978-3-319-24574-4 28.

De Ruijter WJ. 1995. Imaging properties and applications of slow-scan charge-coupled device cameras suitable for electron microscopy. Micron. 26(3):247–275. doi:10.1016/0968-4328(95)00054-8.

Ruskin RS, Yu Z, Grigorieff N. 2013. Quantitative characterization of electron detectors for transmission electron microscopy. J Struct Biol. 184(3):385–393. doi:10.1016/j.jsb.2013.10.016. http://dx.doi.org/10.1016/j.jsb.2013.10.016.

Salvat F, Fernandez-Varea JM, Sempau J. PENELOPE2006, A Code System for Monte-Carlo Simulation of Electron and Photon Transport.

http://inis.iaea.org/search/search.aspx?orig_q=RN:41016798.

van Schayck JP, van Genderen E, Maddox E, Roussel L, Boulanger H, Fröjdh E, Abrahams JP, Peters PJ, Ravelli RBG. 2020. Sub-pixel electron detection using a convolutional neural network. Ultramicroscopy. 218(August):113091. doi:10.1016/j.ultramic.2020.113091. https://doi.org/10.1016/j.ultramic.2020.113091.

Sun M, Azumaya CM, Tse E, Bulkley DP, Harrington MB, Gilbert G, Frost A, Southworth D, Verba KA, Cheng Y, et al. 2021. Practical considerations for using K3 cameras in CDS mode for high-resolution and high-throughput single particle cryo-EM. J Struct Biol. 213(3):107745. doi:https://doi.org/10.1016/j.jsb.2021.107745.

https://www.sciencedirect.com/science/article/pii/S1047847721000502.

Tate MW, Purohit P, Chamberlain D, Nguyen KX, Hovden R, Chang CS, Deb P, Turgut E, Heron JT, Schlom DG, et al. 2016. High Dynamic Range Pixel Array Detector for Scanning Transmission Electron Microscopy. Microsc Microanal. 22(1):237–249.

doi:10.1017/S1431927615015664. https://doi.org/10.1017/S1431927615015664.

Tim Pennycook & Christoph Hofer. 2021. PyPtychoSTEM.

https://gitlab.com/pyptychostem/pyptychostem.

Wang J, Zhu H, Wang S-H, Zhang Y-D. 2021. A Review of Deep Learning on Medical Image Analysis. Mob Networks Appl. 26(1):351–380. doi:10.1007/s11036-020-01672-7. https://doi.org/10.1007/s11036-020-01672-7.

Wu J. 2018. Complexity and accuracy analysis of common artificial neural networks on pedestrian detection. MATEC Web Conf. 232. doi:10.1051/matecconf/201823201003.

Zhang S, Wen L, Bian X, Lei Z, Li SZ. 2018. Occlusion-Aware R-CNN: Detecting Pedestrians in a Crowd. Lect Notes Comput Sci (including Subser Lect Notes Artif Intell Lect Notes Bioinformatics). 11207 LNCS:657–674. doi:10.1007/978-3-030-01219-9 39.

Bammes B, Ramachandra R, Mackey MR, Bilhorn R, Ellisman M. 2019. Multi-Color Electron Microscopy of Cellular Ultrastructure Using 4D-STEM. Microsc Microanal. 25(S2):1060–1061. doi:10.1017/S1431927619006032. https://doi.org/10.1017/S1431927619006032.

Battaglia M, Contarato D, Denes P, Giubilato P. 2009. Cluster imaging with a direct detection CMOS pixel sensor in Transmission Electron Microscopy. Nucl Instruments Methods Phys Res Sect A Accel Spectrometers, Detect Assoc Equip. 608(2):363–365.

doi:10.1016/j.nima.2009.07.017. http://dx.doi.org/10.1016/j.nima.2009.07.017.

Blaiszik B, Scourtas A, Schmidt K. 2022. Foundry. https://github.com/MLMI2-CSSI/foundry.

Chatterjee D, Wei J, kvit A, Bammes B, Levin B, Bilhorn R, Voyles P. 2021. An Ultrafast Direct Electron Camera for 4D STEM. Microsc Microanal. 27(S1):1004–1006. doi:10.1017/S1431927621003809.

Datta A, Ng KF, Balakrishnan D, Ding M, Chee SW, Ban Y, Shi J, Loh ND. 2021. A data reduction and compression description for high throughput time-resolved electron microscopy. Nat Commun. 12(1):1–15. doi:10.1038/s41467-020-20694-z.

Grigorescu S, Trasnea B, Cocias T, Macesanu G. 2020. A survey of deep learning techniques for autonomous driving. J F Robot. 37(3):362–386. doi:https://doi.org/10.1002/rob.21918. https://doi.org/10.1002/rob.21918.

He L, Ren X, Gao Q, Zhao X, Yao B, Chao Y. 2017. The connected-component labeling problem: A review of state-of-the-art algorithms. Pattern Recognit. 70:25–43. doi:https://doi.org/10.1016/j.patcog.2017.04.018.

https://www.sciencedirect.com/science/article/pii/S0031320317301693.

Jacobs R. 2022. Deep learning object detection in materials science: Current state and future directions. Comput Mater Sci. 211(May):111527. doi:10.1016/j.commatsci.2022.111527. https://doi.org/10.1016/j.commatsci.2022.111527.

Jocher G, Chaurasia A, Qiu J. 2023. YOLO by Ultralytics.

https://github.com/ultralytics/ultralytics.

Levin BDA. 2021. Direct detectors and their applications in electron microscopy for materials science. JPhys Mater. 4(4). doi:10.1088/2515-7639/ac0ff9.

Li X, Mooney P, Zheng S, Booth CR, Braunfeld MB, Gubbens S, Agard DA, Cheng Y. 2013. Electron counting and beam-induced motion correction enable near-atomic-resolution single-particle cryo-EM. Nat Methods. 10(6):584–590. doi:10.1038/nmeth.2472.

Li X, Zheng SQ, Egami K, Agard DA, Cheng Y. 2013. Influence of electron dose rate on electron counting images recorded with the K2 camera. J Struct Biol. 184(2):251–260. doi:10.1016/j.jsb.2013.08.005. http://dx.doi.org/10.1016/j.jsb.2013.08.005.

Liu Y, Sun P, Wergeles N, Shang Y. 2021. A survey and performance evaluation of deep learning methods for small object detection. Expert Syst Appl. 172:114602. doi:10.1016/J.ESWA.2021.114602.

Mahr C, Müller-Caspary K, Grieb T, Schowalter M, Mehrtens T, Krause FF, Zillmann D, Rosenauer A. 2015. Theoretical study of precision and accuracy of strain analysis by nano-beam electron diffraction. Ultramicroscopy. 158:38–48. doi:10.1016/j.ultramic.2015.06.011. http://dx.doi.org/10.1016/j.ultramic.2015.06.011.

maintainers T, contributors. 2016. TorchVision: PyTorch's Computer Vision library. GitHub Repos.

McMullan G., Chen S, Henderson R, Faruqi AR. 2009. Detective quantum efficiency of electron area detectors in electron microscopy. Ultramicroscopy. 109(9):1126–1143. doi:10.1016/j.ultramic.2009.04.002.

McMullan G, Clark AT, Turchetta R, Faruqi AR. 2009. Enhanced imaging in low dose electron microscopy using electron counting. Ultramicroscopy. 109(12):1411–1416. doi:https://doi.org/10.1016/j.ultramic.2009.07.004.

https://www.sciencedirect.com/science/article/pii/S0304399109001703.

McMullan G, Faruqi AR, Clare D, Henderson R. 2014. Comparison of optimal performance at 300keV of three direct electron detectors for use in low dose electron microscopy.

Ultramicroscopy. 147:156–163. doi:10.1016/j.ultramic.2014.08.002.

http://dx.doi.org/10.1016/j.ultramic.2014.08.002.

Mendez JH, Mehrani A, Randolph P, Staggb S. 2019. Throughput and resolution with a next-generation direct electron detector. IUCrJ. 6:1007–1013. doi:10.1107/S2052252519012661.

Meyer RR, Kirkland AI. 2000. Characterisation of the signal and noise transfer of CCD cameras for electron detection. Microsc Res Tech. 49(3):269–280.

doi:https://doi.org/10.1002/(SICI)1097-0029(20000501)49:3<269::AID-JEMT5>3.0.CO;2-B. https://doi.org/10.1002/(SICI)1097-0029(20000501)49:3%3C269::AID-JEMT5%3E3.0.CO.

Mir JA, Clough R, MacInnes R, Gough C, Plackett R, Shipsey I, Sawada H, MacLaren I, Ballabriga R, Maneuski D, et al. 2017. Characterisation of the Medipix3 detector for 60 and 80 keV electrons. Ultramicroscopy. 182:44–53. doi:10.1016/j.ultramic.2017.06.010. http://dx.doi.org/10.1016/j.ultramic.2017.06.010.

Nakane T, Kotecha A, Sente A, McMullan G, Masiulis S, Brown PMGE, Grigoras IT, Malinauskaite L, Malinauskas T, Miehling J, et al. 2020. Single-particle cryo-EM at atomic resolution. Nature. 587(7832):152–156. doi:10.1038/s41586-020-2829-0. https://doi.org/10.1038/s41586-020-2829-0.

Neubeck A, Van Gool L. 2006. Efficient Non-Maximum Suppression. In: 18th International Conference on Pattern Recognition (ICPR'06). Vol. 3. p. 850–855.

Paton KA, Veale MC, Mu X, Allen CS, Maneuski D, Kübel C, O'Shea V, Kirkland AI, McGrouther D. 2021. Quantifying the performance of a hybrid pixel detector with GaAs:Cr sensor for transmission electron microscopy. Ultramicroscopy. 227(February). doi:10.1016/j.ultramic.2021.113298.

Peng R, Fu X, Mendez JH, Randolph PS, Bammes BE, Stagg SM. 2023. Characterizing the resolution and throughput of the Apollo direct electron detector. J Struct Biol X. 7:100080. doi:https://doi.org/10.1016/j.yjsbx.2022.100080.

https://www.sciencedirect.com/science/article/pii/S2590152422000216.

Peng X, Pelz PM, Zhang Q, Chen P, Cao L, Zhang Y, Liao H-G, Zheng H, Wang C, Sun S-G, et al. 2022. Observation of formation and local structures of metal-organic layers via complementary electron microscopy techniques. Nat Commun. 13(1):5197. doi:10.1038/s41467-022-32330-z. https://doi.org/10.1038/s41467-022-32330-z.

Pennycook TJ, Lupini AR, Yang H, Murfitt MF, Jones L, Nellist PD. 2015. Efficient phase contrast imaging in STEM using a pixelated detector. Part 1: Experimental demonstration at atomic resolution. Ultramicroscopy. 151:160–167. doi:10.1016/j.ultramic.2014.09.013.

Plotkin-Swing B, Corbin GJ, De Carlo S, Dellby N, Hoermann C, Hoffman M V, Lovejoy TC, Meyer CE, Mittelberger A, Pantelic R, et al. 2020. Hybrid pixel direct detector for electron energy loss spectroscopy. Ultramicroscopy. 217:113067.

doi:https://doi.org/10.1016/j.ultramic.2020.113067.

https://www.sciencedirect.com/science/article/pii/S0304399120302187.

Ren S, He K, Girshick R, Sun J. 2017. Faster R-CNN: Towards Real-Time Object Detection

with Region Proposal Networks. IEEE Trans Pattern Anal Mach Intell. 39(6):1137–1149. doi:10.1109/TPAMI.2016.2577031.

Rodenburg J, Bates RHT. 1992. The theory of super-resolution electron microscopy via Wigner-distribution deconvolution. Philos Trans R Soc London Ser A Phys Eng Sci. 339:521–553.

Ronneberger O, Fischer P, Brox T. 2015. U-net: Convolutional networks for biomedical image segmentation. Lect Notes Comput Sci (including Subser Lect Notes Artif Intell Lect Notes Bioinformatics). 9351:234–241. doi:10.1007/978-3-319-24574-4 28.

De Ruijter WJ. 1995. Imaging properties and applications of slow-scan charge-coupled device cameras suitable for electron microscopy. Micron. 26(3):247–275. doi:10.1016/0968-4328(95)00054-8.

Ruskin RS, Yu Z, Grigorieff N. 2013. Quantitative characterization of electron detectors for transmission electron microscopy. J Struct Biol. 184(3):385–393. doi:10.1016/j.jsb.2013.10.016. http://dx.doi.org/10.1016/j.jsb.2013.10.016.

Salvat F, Fernandez-Varea JM, Sempau J. PENELOPE2006, A Code System for Monte-Carlo Simulation of Electron and Photon Transport.

http://inis.iaea.org/search/search.aspx?orig_q=RN:41016798.

van Schayck JP, van Genderen E, Maddox E, Roussel L, Boulanger H, Fröjdh E, Abrahams JP, Peters PJ, Ravelli RBG. 2020. Sub-pixel electron detection using a convolutional neural network. Ultramicroscopy. 218(August):113091. doi:10.1016/j.ultramic.2020.113091. https://doi.org/10.1016/j.ultramic.2020.113091.

Sun M, Azumaya CM, Tse E, Bulkley DP, Harrington MB, Gilbert G, Frost A, Southworth D, Verba KA, Cheng Y, et al. 2021. Practical considerations for using K3 cameras in CDS mode for high-resolution and high-throughput single particle cryo-EM. J Struct Biol. 213(3):107745. doi:https://doi.org/10.1016/j.jsb.2021.107745.

https://www.sciencedirect.com/science/article/pii/S1047847721000502.

Tate MW, Purohit P, Chamberlain D, Nguyen KX, Hovden R, Chang CS, Deb P, Turgut E, Heron JT, Schlom DG, et al. 2016. High Dynamic Range Pixel Array Detector for Scanning Transmission Electron Microscopy. Microsc Microanal. 22(1):237–249. doi:10.1017/S1431927615015664. https://doi.org/10.1017/S1431927615015664.

Tim Pennycook & Christoph Hofer. 2021. PyPtychoSTEM.

https://gitlab.com/pyptychostem/pyptychostem.

Wang J, Zhu H, Wang S-H, Zhang Y-D. 2021. A Review of Deep Learning on Medical Image Analysis. Mob Networks Appl. 26(1):351–380. doi:10.1007/s11036-020-01672-7. https://doi.org/10.1007/s11036-020-01672-7.

Wu J. 2018. Complexity and accuracy analysis of common artificial neural networks on pedestrian detection. MATEC Web Conf. 232. doi:10.1051/matecconf/201823201003.

Zhang S, Wen L, Bian X, Lei Z, Li SZ. 2018. Occlusion-Aware R-CNN: Detecting Pedestrians in a Crowd. Lect Notes Comput Sci (including Subser Lect Notes Artif Intell Lect Notes Bioinformatics). 11207 LNCS:657–674. doi:10.1007/978-3-030-01219-9 39.

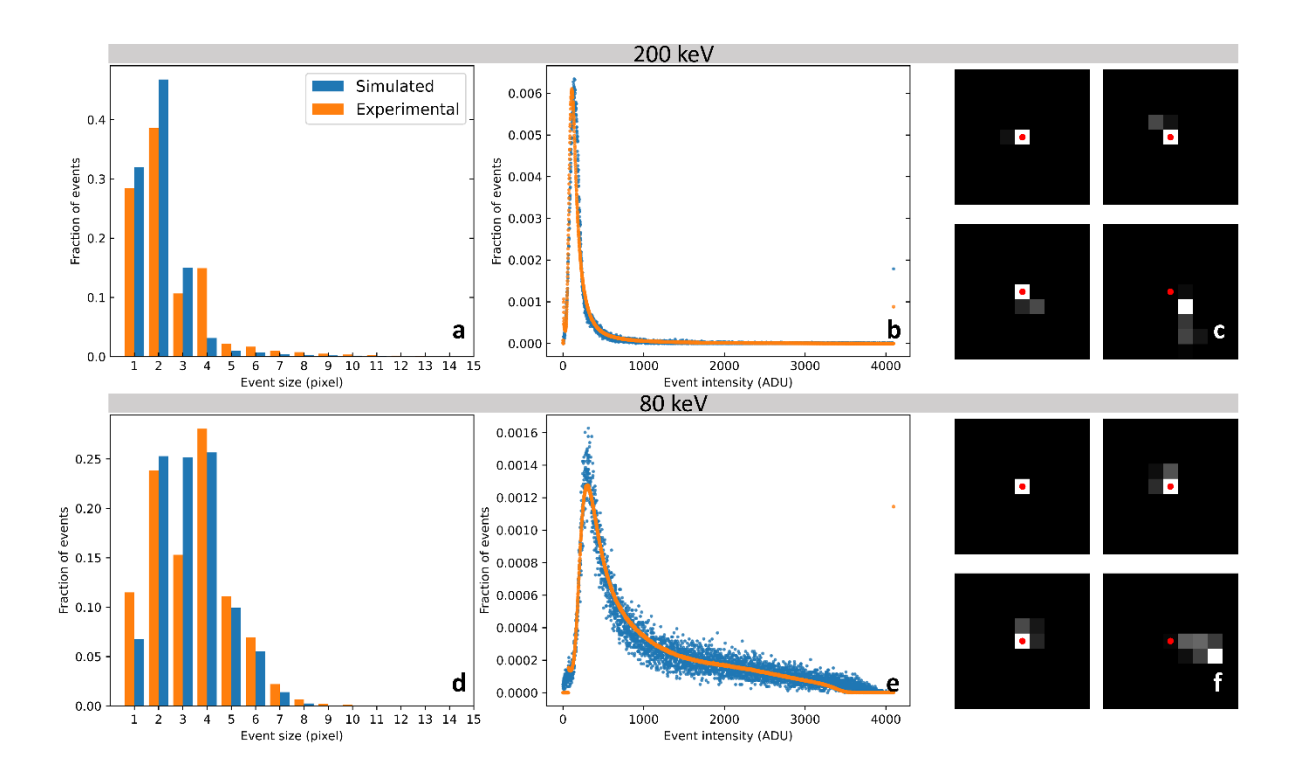


Figure 1. Validation of simulated electron event images. (a-c) Event size distribution, event intensity distribution, and example single-electron event patterns for 200 kV electrons and (d-f) 80 kV electrons.

Table 1. Parameters of the Faster R-CNN model and the training process.

Hyperparameters	Value	Training parameters	Value
RPN foreground IoU threshold	0.6	Epoch	10
RPN background IoU threshold	0.3	Batch size (Image)	1
RPN Pre-NMS top detection	800, or tuned	Learning rate	0.0001-0.001
number			

RPN Post-NMS top detection number	400, or tuned	Weight decay	0.0001
RPN NMS threshold	0.2	Momentum	0.9
Classifier foreground IoU threshold	0.1	RPN batch size per image	256
Classifier background IoU threshold	0.1	RPN positive fraction	0.5
Classifier NMS threshold	0.02	Classifier batch size pointinge	er 128
Classifier score threshold	0.1, or tuned	Classifier positive fraction	0.75
Classifier detections per image	200, or tuned	RPN regression weights / Classifier regression weights	(1, 1, 1, 1)

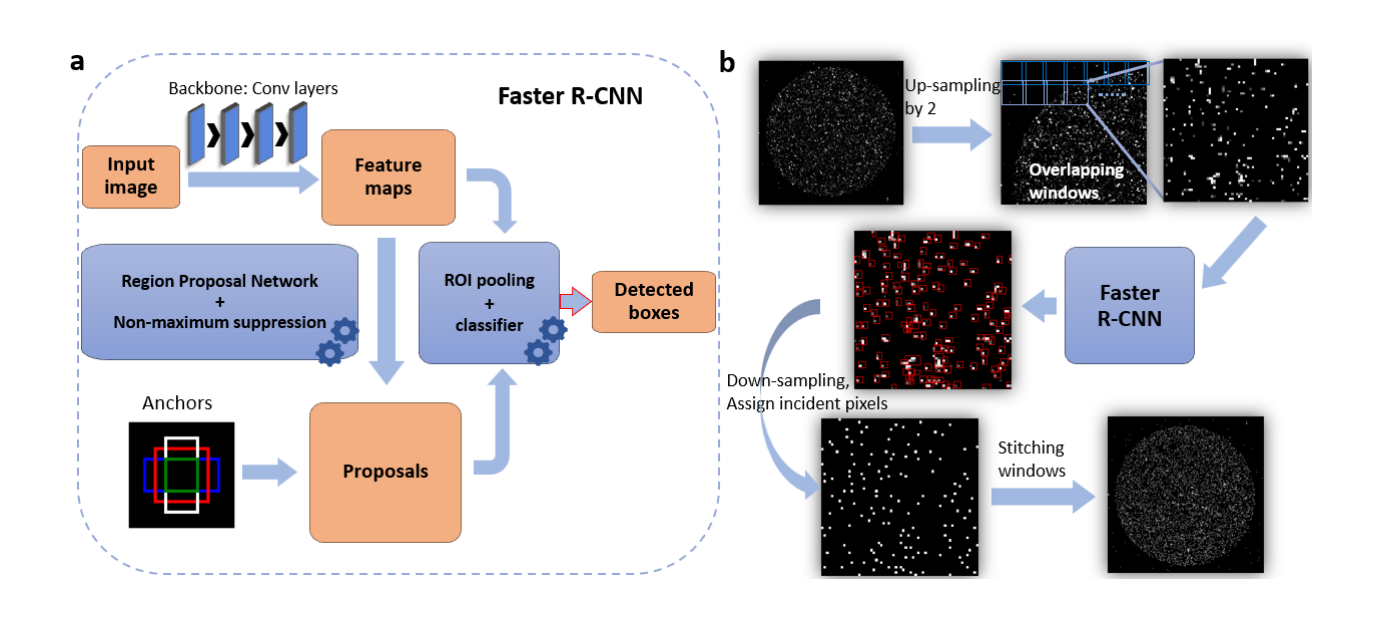


Figure 2. Schematic of the deep learning approach toward counting single electron event from detector readout. (a) Schematic of components of the Faster R-CNN model. (b) schematic of the workflow for applying the electron counting model.

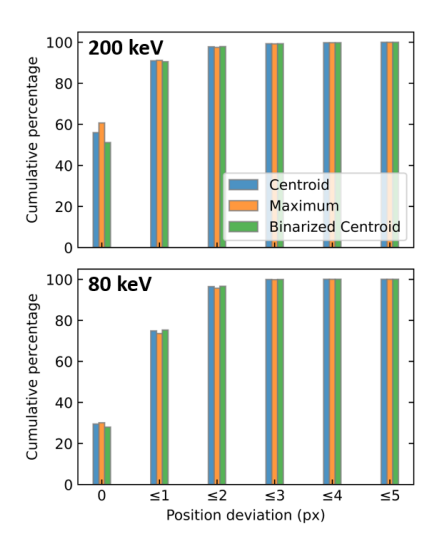


Figure 3. Cumulative distribution of the deviation between the positions of the electron strike determined by various methods and the true position, calculated from simulated electron events at 200 keV (top) and 80 keV (bottom).

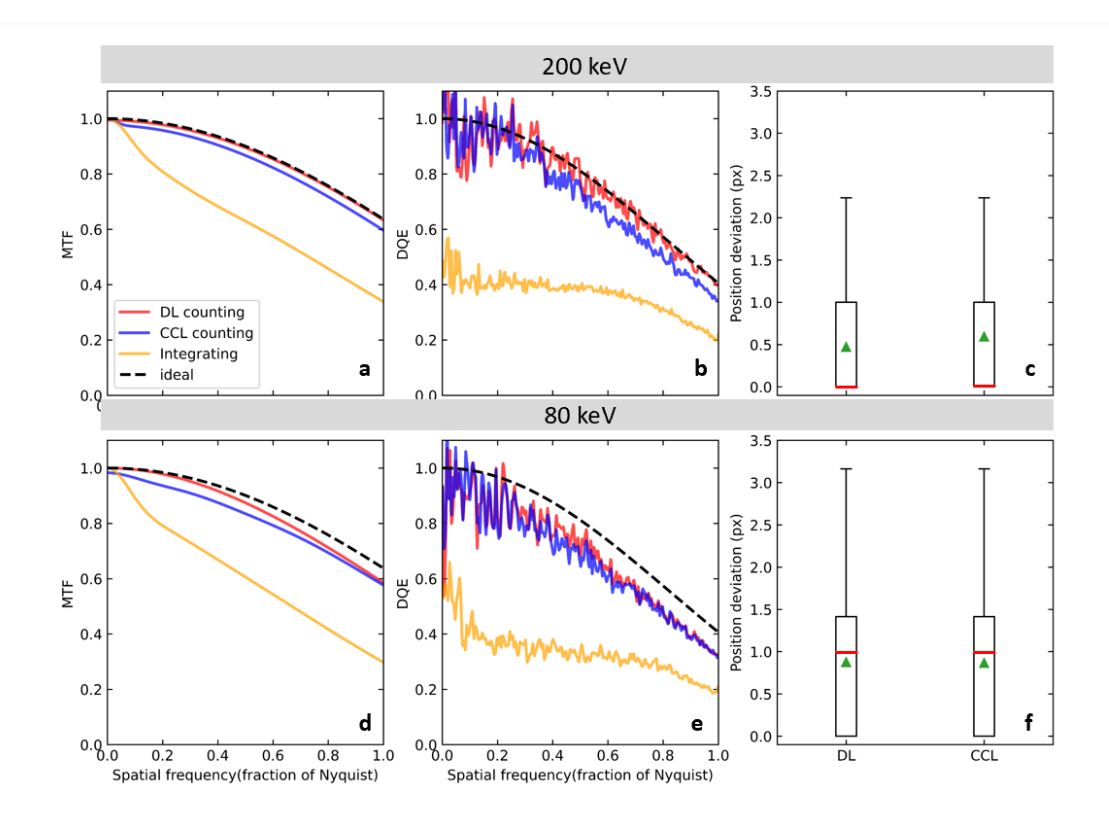


Figure 4. MTF and DQE calculated using experimental data and position deviation calculated from simulated data. (a-c) For 200 keV, (d-f) for 80 keV. In (c) and (f), the green triangle represents the mean, the red line represents the median, the box represents the first quantile and third quantile.

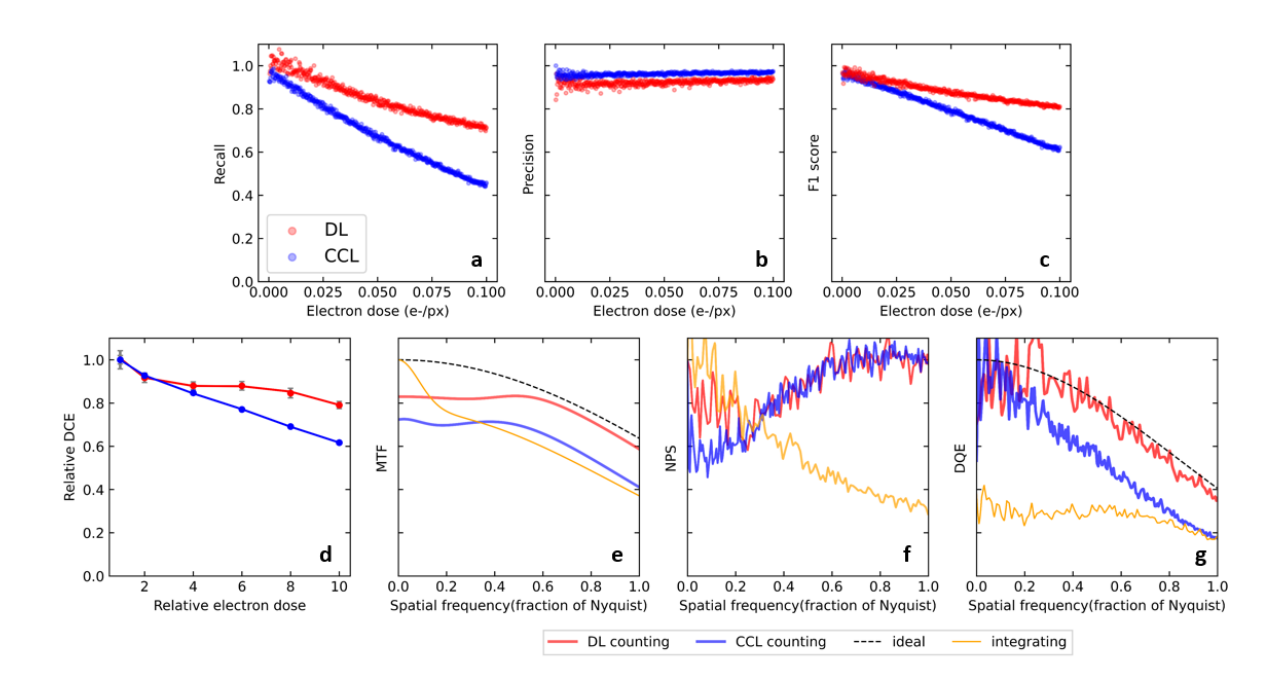


Figure 5. Performance of the DL model and CCL at increased dose rate. (a-c) recall, precision, and F1 score calculated from simulated data at 200 keV, (d-g) relative DCE, MTF, NPS and DQE calculated on experimental data at 200 keV. The NPS curves were normalized by an averaged value at high frequency. MTF, NPS, and DQE are shown for an electron density of 0.06 e⁻ / pixel.

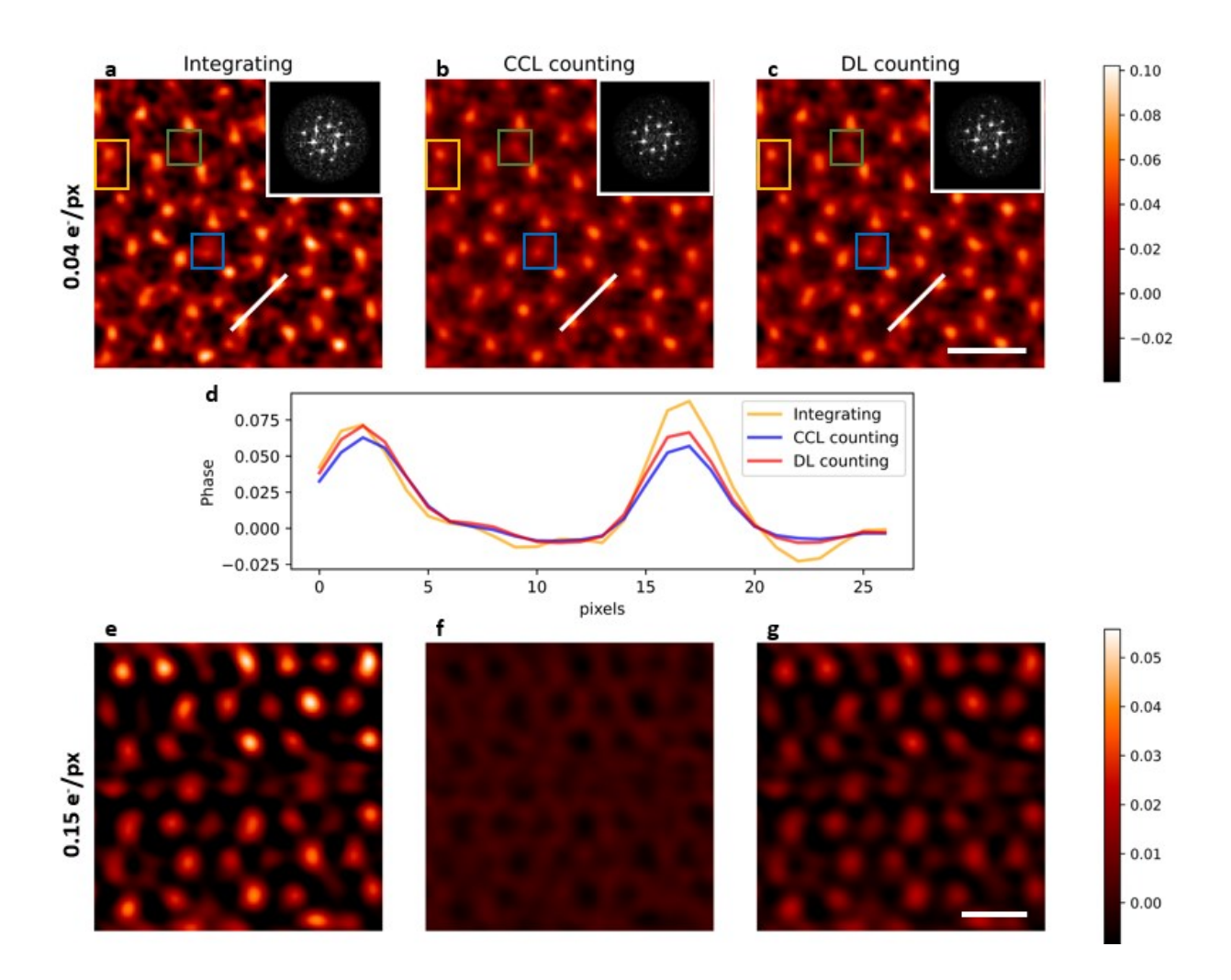


Figure 6. Comparison of reconstructed phase images from original integrating dataset, dataset processed with counting using CCL, and dataset processed with counting using the DL model. (a-c) Phase images reconstructed from the data collected with a moderately high electron dose. The boxes indicate positions where atoms in the counted dataset are better resolved relative to the integrated dataset. The diffractogram intensities are inserted for each phase. (d) compares the line profiles along the white lines in (a-c). (e-f) Phase images reconstructed from the data collected at higher electron dose rate, which is challenging for conventional counting methods. Scale bar is 5 Å.

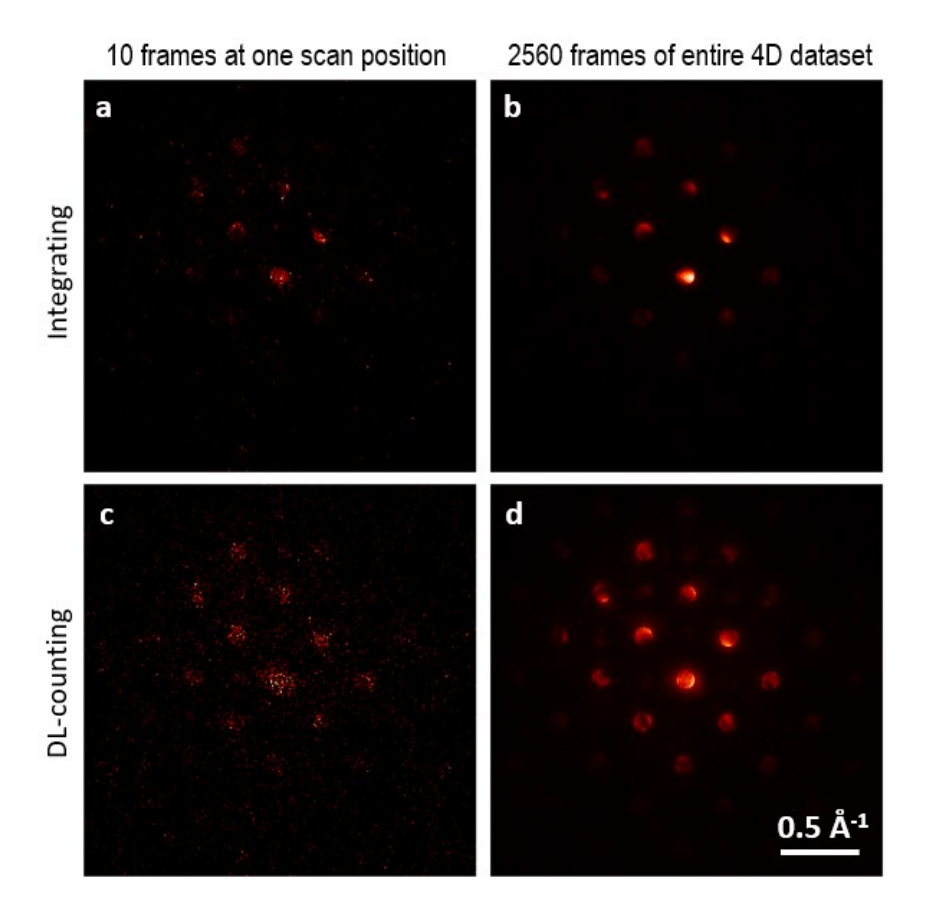


Figure 7. Comparison of CBED pattern images taken from a 4D STEM data set for unstrained SrTiO₃ [001], where the electron density inside the zero disk is about 0.3 e⁻/pixel. (a, c) summed over 10 frames recorded at one probe position. (b, d) summer over all 2560 frames of the 4D STEM dataset at 256 probe positions. (a) and (b) integrating mode data. (c) and (d) data summed after DL model counting. The CCL counting method failed at images with such high local electron density, so those results are not shown.